Materials Advances

ROYAL SOCIETY OF CHEMISTRY

PAPER

View Article Online
View Journal

Cite this: DOI: 10.1039/d5ma01181g

Temperature- and atmosphere-driven phase evolution in sol–gel synthesized barium nickelate powders

Ian C. Graham, [a] Jeong-Woo Sun, [a] Kayla Y. Chuong, [a] Anna M. Österholm [ab] and Lauren M. Garten *[a]

Received 12th October 2025,
Accepted 13th April 2026

DOI: 10.1039/d5ma01181g

rsc.li/materials-advances

Controlling phase formation and stoichiometry in barium nickelate (BNO, $BaNiO_{3-x}$) is critical for the development of high-performance BNO-based catalysts, gas sensors, and piezoelectrics. The multiple oxidation states of nickel (Ni^{2+}, Ni^{3+}, and Ni^{4+}) are thought to enable the broad range of BNO phases: however, the conditions that selectively access these phases and the stoichiometric ranges each phase accommodates remain unclear. This study presents a systematic calcination approach to map the relationship between calcination temperature, oxygen atmosphere, BNO phase, morphology, and stoichiometry. BNO sol–gels calcined from 800 to 1000 °C under controlled oxygen flow (0–3 L min^{-1}) reveal a phase-selective synthesis window: oxygen-rich calcination at 800 °C produces the piezoelectric $P6_3mc$ phase, and higher temperatures promote formation of the metastable piezoelectric $R32$ phase and drive the phase transition to a previously unassigned BNO. In contrast, under oxygen-free conditions, calcination above 800 °C yields the centrosymmetric $P6_3/mmc$ phase. Increasing the temperature and oxygen flow also drives the transition from a porous to a dendritic morphology, increases crystallite size, and tunes stoichiometry from $BaNi_{0.93}O_{2.76}$ to $BaNi_{0.91}O_{2.24}$. These findings offer a framework for controlling BNO phase formation, morphology, and stoichiometry, providing a broadly applicable strategy for synthesizing complex multivalent oxides and enabling the design of BNO-based catalysts, gas sensors, and piezoelectrics.

Introduction

Barium nickelate (BNO) holds significant potential for catalysis, gas sensing, and lead-free piezoelectrics, but realizing the full potential of this material requires a deeper understanding of the relationship between stoichiometry and crystalline phases. Due to the multiple accessible oxidation states of nickel (Ni^{2+}, Ni^{3+}, and Ni^{4+}), BNO can accommodate a broad range of oxygen stoichiometries.[1–9] Barium nickelate is reported to have stoichiometries that span continuously from $BaNiO_2$, where nickel is in the Ni^{2+} state, to $BaNiO_3$, where nickel is in the rare Ni^{4+} state.[10] The relationship between the ground state crystal structures and stoichiometry has yet to be established for many of these materials. For instance, $BaNiO_3$ adopts the $P6_3/mmc$ space group, while the orthorhombic $Cmcm$ phase has been reported for $BaNiO_2$.[2,11] For many of the compositions that lie between these end member compounds, the stable phase is not yet determined. Notably, the rarely observed h-$BaNiO_{2.36}$ has yet to have its space group identified.[12,13] Furthermore, there are phases, such as the rare $R32$ phase or the theoretically predicted $Pm\bar{3}m$ phase, where a broad range of stoichiometries is expected but has not been experimentally confirmed.[3,5–9] The $R32$ and $Pm\bar{3}m$ phases are particularly interesting for electrocatalysis, as both phases are predicted to be conducive to enabling enhanced redox reactions at the surface.[5–9,14] Many stoichiometric compositions, such as $BaNiO_3$, also exhibit multiple polymorphs ($P6_3/mmc$ and $P6_3mc$).[1,2] Breaking the center of symmetry when transitioning from the centrosymmetric $P6_3/mmc$ phase into the non-centrosymmetric $P6_3mc$ or $R32$ phases allows for the emergence of properties absent in the ground state, such as piezoelectricity, second harmonic generation, and ferroelectricity.[15] Understanding how to select between phases or polymorphs, or how to control the oxygen stoichiometry within a single phase is critical for increasing the catalytic activity of BNO, as well as implementing BNO in piezoelectric applications. Establishing how variations in BNO stoichiometry correlate with the phase will provide critical insights into the structure–property relationships needed to control phase formation pathways,

[a] School of Materials Science and Engineering, Georgia Institute of Technology, 30332, Atlanta, GA, USA. E-mail: lauren.garten@mse.gatech.edu
[b] School of Chemistry & Biochemistry, Georgia Institute of Technology, 30332, Atlanta, GA, USA

enabling the targeted selection of phases to reach the full potential of BNO applications. For example, understanding the structure–property–stoichiometry relationship will enable the advancement of BNO as an oxygen evolution reaction (OER) catalyst, as reduction in the Ni oxidation state (reduction in oxygen stoichiometry) has been suggested to increase OER catalytic activity.[14]

Accessing the broad range of stoichiometries in BNO requires a processing method with oxygen atmosphere tunability. $BaNiO_3$ has previously been synthesized *via* molten-salt crystal growth, solid-state ceramic processing, and sol–gel solution processing.[1,16–18] The sol–gel synthesis of BNO was first reported by Lee *et al.*, who elucidated the impact of sol–gel pH on BNO phase formation and BNO powder morphology at a calcination temperature of 900 °C in air.[18] Sol–gel solution synthesis is a particularly promising route as it allows for precursor optimization, which enables precise control over the stoichiometry, homogeneity, and particle size of the resulting product.[19,20] Furthermore, sol–gel solution synthesis also enables the use of a range of oxidative atmospheres during the calcination step. Varying the calcination environment offers broad control over oxygen activity during crystallization, which, as we will show, leads to a wide range of oxygen stoichiometries in the final powder.[21,22]

This work advances the understanding of the phase–stoichiometry relationship in sol–gel solution BNO powders by investigating how calcination temperature and atmosphere impact phase formation, stoichiometry and powder morphology. We hypothesize that decreasing oxygen activity, *via* higher calcination temperature or lower oxygen partial pressure, will drive a phase transition from the $P6_3/mmc$ and $P6_3mc$ phases to the $R32$ and $Cmcm$ BNO phases as longer Ni–O bonds and lower Ni coordination favor lower Ni oxidation states. To test this hypothesis, dried BNO gels were calcined at 800–1000 °C under oxygen flow rates of 0–3 L min^{-1}. X-ray diffraction (XRD), scanning electron microscopy (SEM), and energy dispersive X-ray spectroscopy (EDS) reveal that calcining above 800 °C induces a transition from $P6_3mc$ to h-$BaNiO_{2.36}$, a shift from a porous sponge to a dendritic morphology, and a reduction in oxygen content from $BaNiO_{2.76}$ to $BaNiO_{2.25}$. These results highlight the critical role of calcination temperature and atmosphere in tuning the structure and composition of BNO, offering insight into how these processing parameters can be leveraged to tailor BNO for a range of potential applications.

Experimental

Barium nickelate (BNO and $BaNiO_{3-x}$) powders were synthesized using a sol–gel method adapted from the work of Lee *et al.* in ref. 18. A brief synopsis of the adapted methods is provided here. $Ba(NO_3)_2$ (Thermo Scientific Chemicals, 99% purity) and $Ni(NO_3)_2{\cdot}6H_2O$ (Thermo Scientific Chemicals, 98% purity) precursors were added to 50 mL of deionized water. Then, 3.0 mL of HNO_3 (Fisher Chemical, TraceMetal Grade) was added to the solution, followed by heating to 70 °C and stirring for 30 min under ambient conditions. Citric acid (Thermo Scientific Chemicals, 99+% purity) was added to the solution, which was left to stir at 70 °C for 1 hour. The pH of the sol–gel was raised to 11 by adding ethylenediamine (Thermo Scientific Chemicals, 99%) to form a citrate gel. In addition to raising the pH/promoting gelation, ethylenediamine reacts with nitric acid to form ethylenediamine dinitrate and therefore prevents the reformation of $Ba(NO_3)_2$. The sol–gels were then dried at 250 °C for 6 hours in a box furnace (Thermo Scientific, Lindberg Blue M) in high-alumina crucibles (Coors Tech). The dried gels were then ground into a powder using a mortar and pestle. The resulting powder was placed in a high-alumina ceramic boat (Coors Tech) for calcination. A tube furnace (SentroTech) with a 3 inch diameter high-alumina tube was used for calcination. The temperature was ramped at 7 °C min^{-1} to calcine at either 800, 900, and 1000 °C. The dwell time for all calcinations was 3 hours. The calcination atmosphere was held constant during each calcination. Between runs the atmosphere was varied between static air and an atmosphere of ultra-high purity oxygen (Airgas, OX UHP300) by varying the oxygen flow rate from 0, 1, 2, or 3 L min^{-1} using an oxygen flow meter (MasterFlex). The oxygen flow rate is reported instead of oxygen partial pressure because the calcination temperature range is higher than the maximum operating temperature for zirconia oxygen partial pressure sensors. Following calcination, the powders were then allowed to cool to room temperature under the same oxygen flow rate used during calcination.

The range of annealing conditions for the BNO powders was determined from *in situ* XRD measurements. To determine the processing window for the formation of BNO, *in situ* XRD measurements were performed using a Rigaku Smartlab XE system with a Cu source (1.5406 Å) operated at 40 kV and 44 mA using a Rigaku Reactor X stage. The dried BNO sol–gels were ramped up to 800 °C at 7 °C min^{-1}, with a dwell time of 3 hours, in flowing air (Airgas) at a flow rate of 80 mL min^{-1}. 2θ measurements were taken at 20 °C and between 250 and 800 °C at 50° increments. The 2θ measurements were conducted with a step size of 0.01° with a scan rate of 4° min^{-1}.

The composition, morphology, and crystal structure of the resulting annealed powders were determined using energy dispersive X-ray spectroscopy (EDS), field emission scanning electron microscopy (FESEM), and X-ray diffraction (XRD), respectively. The EDS measurements were performed on an Axia ChemiSEM (ThermoFisher Scientific) by placing the BNO powders on double sided carbon tape. Ten separate powder samples were analyzed for each annealing condition using a 20.00 kV accelerating voltage and a spot size of 4.0 mm. The resulting atomic percentages from the EDS measurements were then averaged, and the stoichiometric ratios of the BNO powders were calculated with respect to the Ba atomic percentage. The atomic percentages obtained from EDS measurements have an associated uncertainty of ±5%.[23] The FESEM micrographs were captured using a Hitachi SU8230 SEM with an accelerating voltage of 5 kV and an emission current of 10 μA. *Ex situ* XRD 2θ measurements were taken on a Rigaku MiniFlex

Powder XRD with a Cu source (1.5406 Å) under a 30 kV voltage at a current of 15 mA. The 2θ XRD measurements were run at a step size of 0.01° and a speed of 3° min^{-1}. Thermogravimetric analysis (TGA) was carried out on a Q600 SDT (TA Instruments) to determine the sintering temperature. BNO powders were ramped up to 1000 °C at 10 °C min^{-1} in 100 mL of flowing N_2 followed by a dwell time of 80 minutes.

Results and discussion

Effects of processing conditions on the phase composition

Calcination temperature is found to play a critical role in the formation of BNO, impacting the phase, crystallinity, stoichiometry, and morphology. The first step to elucidate the impact of temperature on the phase formation pathways in BNO was to identify the temperature at which BNO begins to form. Temperature-dependent *in situ* X-ray diffractograms (XRD) obtained on dried BNO sol–gels are shown in Fig. S1. The first phase to form upon heating in 80 mL min^{-1} of flowing air is $BaCO_3$ (BCO, CIF # 00-045-1471).[24] Below 800 °C, no diffraction peaks attributable to any crystalline phases of BNO are observed. Above 800 °C, clear signatures of the centrosymmetric $P6_3/mmc$ phase (CIF # 04-006-8338), the non-centrosymmetric $P6_3mc$ phase (CIF # 04-007-8462), and the h-$BaNiO_{2.36}$ phase (space group unknown, CIF # 00-047-0089) of BNO emerge.[1,2,13] The stabilization of BNO is accompanied by a significant reduction in barium carbonate and nickel oxide, leaving only trace amounts in samples calcined above 800 °C. While *in situ* XRD offers valuable real-time insights, its resolution limits precise differentiation between closely related BNO phases such as $P6_3mc$ and $P6_3/mmc$. To overcome this, higher-resolution *ex situ* XRD was employed to enable more definitive phase identification. Accordingly, all subsequent diffraction analyses were conducted *ex situ*, focusing on calcination temperatures between 800 and 1000 °C to capture key phase transformations and the structural evolution in BNO.

The oxygen flow rate is also found to play a critical role in the formation of BNO as it controls phase stability and powder morphology. To assess the BNO phase formation, the oxygen flow rate is increased from 0 to 3 L min^{-1} at temperatures ranging from 800 °C to 1000 °C. The full set of X-ray diffraction patterns for the powders calcined under oxygen flow rates of 0–3 L min^{-1} at calcination temperatures of 800 °C, 900 °C, and 1000 °C can be found in Fig. S2–S4, respectively. Isolating the processing conditions needed to access each phase allows for the determination of the range of stoichiometries and morphologies that each phase can adopt. Mapping the stoichiometry for each phase is a critical step towards directing the phase formation pathway to select between compositions and polymorphs of BNO.

Given that accessing fully oxidized $BaNiO_3$ requires stabilizing nickel in the rare, high Ni^{4+} oxidation state, initial work focuses on calcining using an oxygen flow rate of 3 L min^{-1} to provide the highest oxygen activity possible within the phase formation region observed by *in situ* XRD. Fig. 1a highlights the characteristic XRD results for a BNO powder calcined at 800 °C in an oxygen flow rate of 3 L min^{-1}. The preponderance of the diffraction peaks fit to the $P6_3mc$ phase of $BaNiO_3$, even though the most thermodynamically stable ground state of BNO is reported to be the $P6_3/mmc$ phase.[5–9] The $P6_3/mmc$ phase is observed in the diffraction pattern but at a significantly smaller phase fraction. Furthermore, smaller percentages of the secondary phases *Pnma* $BaCO_3$ and $Fm\bar{3}m$ NiO (CIF # 00-047-1049) are also present.[25] The competition between BNO and $BaCO_3$ + NiO indicates that a calcination temperature of 800 °C is not sufficiently high to overcome the thermodynamic stability of these secondary phases, warranting exploration of higher calcination temperatures.

Increasing the calcination temperature to 900 °C induces the formation of the h-$BaNiO_{2.36}$ phase of BNO, as shown in Fig. 1b.

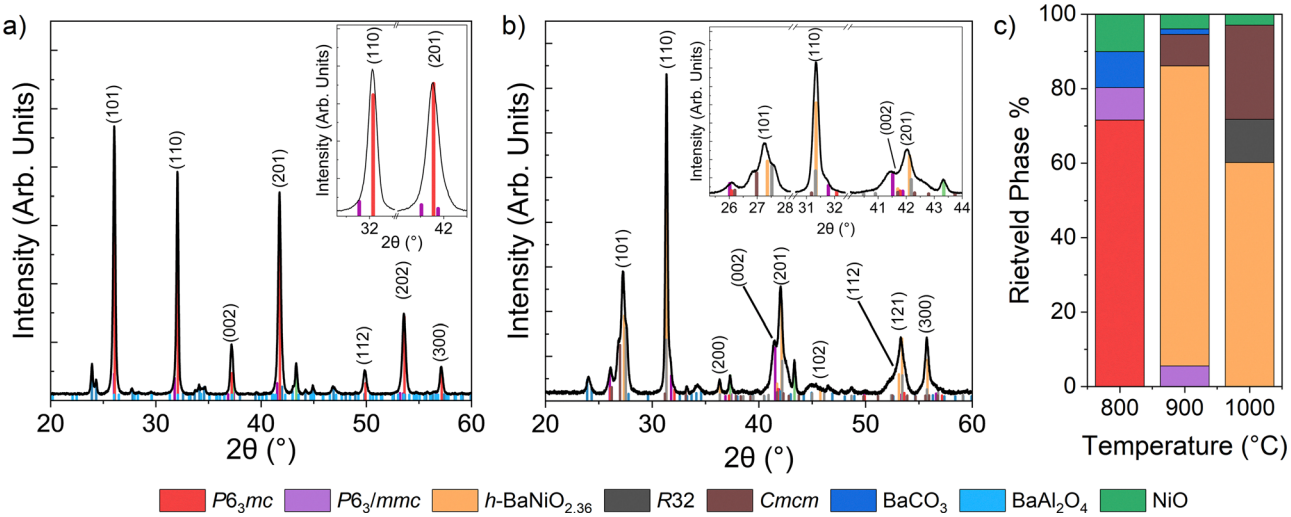

Fig. 1 (a) XRD data of powders calcined at 800 °C at an oxygen flow rate of 3 L min^{-1}. (b) XRD data of powders calcined at 900 °C at an oxygen flow rate of 3 L min^{-1}. (c) Rietveld refinement derived phase percentages of powders calcined at temperatures ranging from 800–1000 °C under an oxygen flow rate of 3 L min^{-1}.

The rare h-$BaNiO_{2.36}$ phase has only been observed twice before in the work of Buttrey *et al.* and Arjomand *et al.*[12,13] Buttrey *et al.* prepared the h-$BaNiO_{2.36}$ phase by mixing $BaCO_3$ and NiO powders and calcining at 1000 °C in air.[13] Arjomand *et al.* obtained the h-$BaNiO_{2.36}$ phase through annealing $BaNiO_{2.5}$ at 900 °C in a muffle furnace.[12] The space group of the h-$BaNiO_{2.36}$ phase has not been previously reported due to persistent phase purity challenges (as such, we refer to the composition of the phase rather than the space group). This work presents the first reports of this phase using a sol–gel solution synthesis route, reaching a phase purity of up to 80.53% for powders sintered at 900 °C. Based on the Miller indices listed in CIF # 00-047-0089 and the systematic absences associated with hexagonal symmetry,[13] the most likely space groups for this phase are either the $P6_3mc$, $P\bar{6}2c$, or $P6_3/mmc$. Further refinements on higher resolution data are required to definitively determine the space group of this material.

In addition to the rare hexagonal phase, we also observe the metastable $R32$ phase of BNO (CIF # 04-009-3992), at a phase fraction of 11.58% for powders calcined at 1000 °C in 3 L min^{-1} of flowing oxygen.[3] Previously, the metastable $R32$ phase of BNO had only been reported once as single crystals in the work of Campá *et al.*[3] Using the powders developed in this work (calcined at 1000 °C in 3 L min^{-1} of O_2, to produce a $BaNi_{0.93}O_{2.68}$ target), we successfully demonstrated the stabilization of the $R32$ phase in thin films using substrate epitaxy *via* pulsed laser deposition (PLD).[26] Although the mechanism underlying the stabilization of the $R32$ phase in the powder is not yet fully understood, its structural similarity to the $P6_3mc$ phase could act as a template to promote stability. Notably, the $R32$ powders exhibit a preferred orientation along the (223) reflection, suggesting either preferential templating effects or morphological alignment during sample preparation for XRD.

The secondary phases $BaCO_3$ and NiO are present in samples calcined at 900 °C, though in notably lower concentrations (5.43% as opposed to 19.63% when calcined at 800 °C). Suppressing the formation of secondary phases with increasing oxygen flow rate has previously been seen in the literature.[27–29] The destabilization of $BaCO_3$ with decreased CO_2 partial pressure (increased oxygen flow) has been observed in the formation of $BaTiO_3$ *via* aqueous chemical solution deposition.[27] Additionally, the reduction of the phase percentage of NiO upon calcination with increased oxygen flow has been previously observed in similar transition metal oxides such as $LiNiO_2$.[28,29]

The $P6_3/mmc$ and $Cmcm$ (CIF # 04-009-9124) phases of BNO are also present after calcination at 900 °C, while diffraction peaks attributable to the $P6_3mc$ phase disappear.[4] Both the $P6_3/mmc$ and $P6_3mc$ phase have previously been attributed to $BaNiO_3$. However, the full range of stoichiometries these phases can adopt is not yet established. The $Cmcm$ phase is attributed to $BaNiO_2$.[4] In the powders calcined at 900 °C, the $P6_3/mmc$ phase persists with similar phase fractions to that in the powders calcined at 800 °C. The temperature-dependent polymorph differentiation suggests that there is a route to selectively target specific polymorphs using solely temperature or subtle changes in oxygen partial pressure during critical stages of formation. Interestingly, both the $P6_3/mmc$ and $Cmcm$ phases of BNO exhibit preferred orientations for the (201) and the (021) planes, respectively. The presence of preferred orientation within the $R32$, $P6_3/mmc$, and $Cmcm$ phases of BNO likely reflects the structural relationship between these phases and the low-temperature $P6_3mc$ phase. At 800 °C, the bounded slow growth directions of the $P6_3mc$ phase are the [101], [110], and [201] directions. The lattice mismatch between the (201) $P6_3mc$ plane and the $P6_3/mmc$ (201) is only 0.65%, whereas the lattice mismatch between the (201) $P6_3mc$ plane and the $Cmcm$ (021) is 4.34%. The lattice mismatch between the $P6_3mc$ (110) and $R32$ (223) planes is 7.29%. The minimal lattice mismatch would support the preferential orientation observed in diffraction peaks attributable to the $P6_3/mmc$ and $Cmcm$ phases, indicating that the $P6_3mc$ phase is the likely starting point along the path of phase formation.

Overall, the XRD results show that the phase transitions of BNO from $P6_3mc$ to $P6_3/mmc$, $R32$, $Cmcm$, and h-$BaNiO_{2.36}$ correlate strongly with the reduction of oxygen activity with increasing temperature. Reducing the oxygen activity leads to the formation of oxygen vacancies, which is documented in analogous complex oxides.[30,31] Oxygen vacancies reduce the oxidation state of Ni, which is better accommodated in phases with longer Ni–O bond lengths – namely the $R32$ and $Cmcm$ phases (and potentially the h-$BaNiO_{2.36}$) – as opposed to the $P6_3mc$ phase.[1,3,4] The BNO phase transitions observed with increasing temperature suggest that once the calcination temperature is raised above a critical point that favors the formation of oxygen vacancies, the $R32$ and $Cmcm$ phases can nucleate off existing $P6_3mc$ crystallites, leading to a preferential orientation.

In order to provide a direct comparison and quantification of the change in the phase configuration with calcination temperature, Rietveld refinements were carried out. The resulting phase percentages and refinement quality metrics (profile factor (R_{wp}), expected factor (R_{exp}), and goodness-of-fit (χ^2)) of the Rietveld refinements are reported in Table S1 in accordance with reporting conventions in previous literature.[32] Fig. 1c provides a comparison of the relative amounts of phases present in the sol–gel powders calcined from 800 to 1000 °C at a constant oxygen flow rate (3 L min^{-1}). The predominant BNO phase at 800 °C is the $P6_3mc$ at 71.57%, followed by the $P6_3/mmc$ at 8.80% with an additional 19.63% of secondary phases ($BaCO_3$ and NiO). Upon increasing the temperature to 900 °C, the predominant phase of BNO transitions to the h-$BaNiO_{2.36}$ phase (80.53%). This transition is driven by an increase in the formation of oxygen vacancies. The $P6_3/mmc$ and $Cmcm$ phases of BNO were present at relative phase percentages of 5.54% and 8.50%, respectively. Additionally, there is a notable reduction in the concentration of secondary phases, from 19.63% to 5.43%, in samples calcined at 900 °C compared to 800 °C powders due to the reduced stability of $BaCO_3$ at higher temperatures. Powders calcined at 1000 °C exhibit a lower relative phase percentage of the rare h-$BaNiO_{2.36}$ (60.26%), a higher percentage of $Cmcm$ (25.30%), and the formation of the metastable $R32$ phase (11.58%), at the expense of disappearance

of the $P6_3/mmc$ phase. This observation reinforces our hypothesis that oxygen-deficient phases are preferentially stabilized at higher temperatures. At 1000 °C, $BaCO_3$ diffraction peaks are absent. In summary, increasing calcination temperature at an oxygen flow rate of 3 L min^{-1} favors the formation of the metastable and rare h-$BaNiO_{2.36}$ and $R32$ phases, while significantly suppressing secondary phase formation.

Given the observed trend towards BNO phases with reduced oxygen stoichiometry as calcination temperature increases, it is worth investigating the direct influence of oxygen flow rate on phase formation. Lowering oxygen flow in the calcination atmosphere presents another effective strategy to promote the formation of oxygen vacancies and control the nickel oxidation state. The specific influence of oxygen flow rate on the concentration of oxygen vacancies during BNO sol–gel synthesis has yet to be determined. Furthermore, the subsequent impact of oxygen vacancies on the crystal structure of BNO is also unknown, underscoring an important gap in the current understanding of phase stability and material properties. A calcination temperature of 800 °C offers the highest oxygen activity of the temperatures at which BNO crystallization occurs, making 800 °C an ideal starting point for varying the calcination atmosphere as it would likely lead to the widest range of oxygen vacancy concentrations. The analysis of the diffraction data of the dried BNO sol–gels calcined at 800 °C at the various oxygen flow rates is shown in Fig. S2. As discussed in connection to Fig. 1c, Rietveld refinements were carried out to obtain relative phase percentages. The resulting phase percentages of the BNO powders calcined under different oxygen flow rates are shown in Fig. 2a. In the absence of flowing oxygen, $BaCO_3$, $BaAl_2O_4$ (CIF # 01-084-4280),[33] and NiO were found to be the sole crystalline phases.

Increasing the oxygen flow rate to 1 L min^{-1} leads to the $P6_3mc$ phase becoming the predominant crystalline phase (51.63%). The $P6_3/mmc$ phase was also present at 19.00%, while the h-$BaNiO_{2.36}$ phase accounted for 5.14%. Increasing the oxygen flow rate to 2 L min^{-1} results in the disappearance of h-$BaNiO_{2.36}$ diffraction peaks and stabilization of the hexagonal $P6_3mc$ and $P6_3/mmc$ phases. The destabilization of the h-$BaNiO_{2.36}$ phase with increasing oxygen flow rate is in accordance with the results in Fig. 1b for decreasing calcination temperature (*i.e.*, higher oxygen activity). Furthermore, the decrease in the $P6_3/mmc$ in favor of $P6_3mc$ with increasing oxygen atmosphere indicates a route to select between these polymorphs. Again, the relatively higher phase percentage of the $P6_3mc$ phase with increasing oxygen flow suggests that higher oxygen activity environments favor this BNO phase. Raising the oxygen flow rate to 3 L min^{-1} further increased the relative phase percentage of the $P6_3mc$ phase of BNO, accompanied by a decrease of the $P6_3/mmc$ phase and the undesirable secondary phases. From the relative phase percentage data presented in Fig. 2a, increasing oxygen activity in the calcination atmosphere is essential for stabilizing BNO over the secondary phases of $BaCO_3$, NiO, and $BaAl_2O_4$.

To further probe the impact of oxygen flow rate on BNO phase formation, BNO sol–gels were calcined at 900 °C and 1000 °C in static air. The relative phase percentages of samples extracted from Rietveld refinements (Table S1) of the powder diffraction measurements (Fig. S3a and S4a) are summarized in Fig. 2b. As the calcination temperature is raised to 900 °C, both

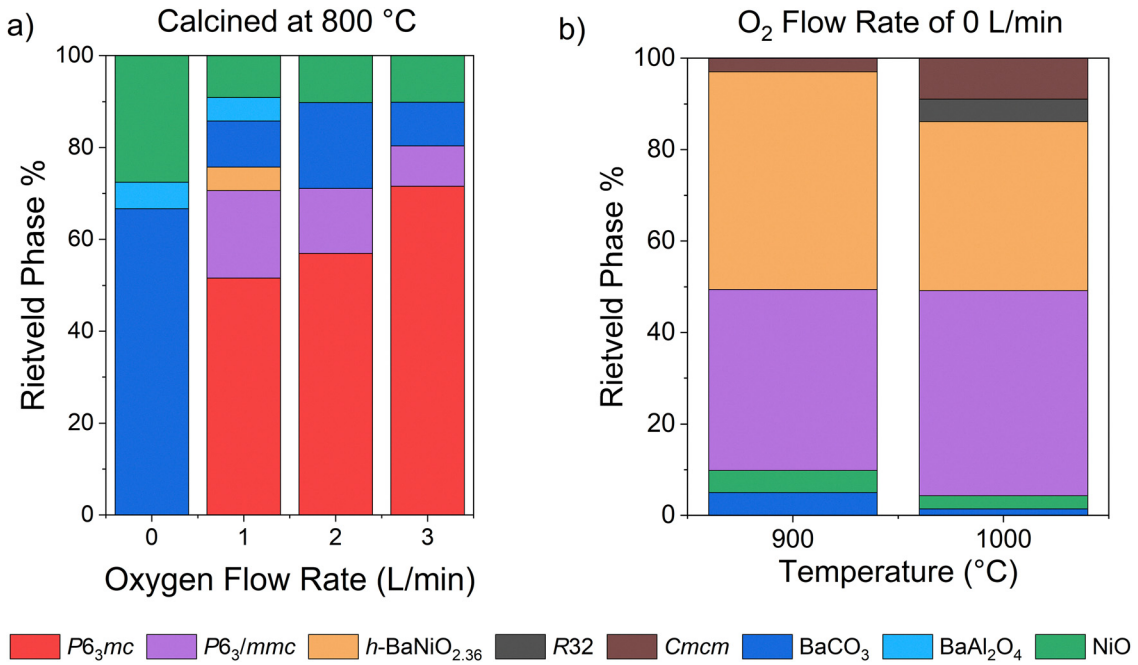

Fig. 2 (a) Rietveld refinement derived phase percentages in the diffraction patterns of BNO gels calcined at 800 °C under oxygen flow rates ranging from 0–3 L min^{-1}. (b) Rietveld refinement derived phase percentages in the diffraction patterns of BNO gels calcined at 900 and 1000 °C under an oxygen flow rate of 0 L min^{-1}.

$P6_3/mmc$ and h-$BaNiO_{2.36}$ phases are observed with relative phase percentages of 39.58% and 47.58%, respectively. The $P6_3mc$ phase is not observed at 900 °C in static air, again supporting that lower oxygen activity environments favor $P6_3/mmc$ over $P6_3mc$.

Raising the calcination temperature to 1000 °C decreases the formation of the h-$BaNiO_{2.36}$ phase, decreasing its relative phase percentage to 37.00%, while increasing the relative phase percentage of $P6_3/mmc$ to 44.90%. Additionally, increasing the calcination temperature to 1000 °C again results in the formation of the metastable $R32$ phase of BNO. The relative phase percentages of $BaCO_3$ and NiO also decrease concurrently. The relative phase percentage results in Fig. 1c and 2b underscore the critical role of flowing oxygen in stabilizing BNO and suppressing the formation of secondary phases. Increasing the oxygen flow rate in the calcination atmosphere reduces the formation of carbonate secondary phases by limiting the reactant, CO_2.[27] Furthermore, increased oxygen flow rate during calcination reduces the formation of Ni^{2+} and therefore reduces the formation of NiO.[28,29] From the results in this work, it is evident that controlling the oxygen activity during calcination is essential in the selection of the BNO stoichiometry and phase.

The calcination of BNO sol–gels over a range of temperatures and oxygen flow rates in this work provides critical insight into the impact of processing conditions on the phase formation of BNO. By analyzing the diffraction results of the calcination experiments at various temperatures and oxygen flow rates, we can begin to map out the phase space of BNO. The relative phase percentages of all BNO phases under all calcination conditions evaluated are summarized in Fig. 3, while Fig. S5 shows the same analysis with the addition of the percentages of all secondary phases. Fig. 3 is overlayed with the stability line for $BaNiO_2$ (adapted from ref. 34); regions below this line correspond to the stability of bulk $BaNiO_2$, while regions above the line represent the stability window for $BaNiO_{3-x}$ ($x < 1$). Several important conclusions can be drawn from these figures:

(1) At all calcination temperatures, increasing oxygen flow increases the stability of BNO over secondary phases.

(2) Increasing the oxygen flow rate from 1 to 3 L min^{-1} increases the relative phase percentage of the $P6_3mc$ polymorph at the expense of the $P6_3/mmc$ phase.

(3) Increasing the oxygen flow rate at calcination temperatures of 900 °C and 1000 °C stabilizes the rare h-$BaNiO_{2.36}$, the metastable $R32$, and $Cmcm$ phases of BNO over the $P6_3/mmc$ phase.

Effects of processing conditions on the crystallite size and morphology

In addition to crystal symmetry, XRD also provides insight into the crystallite size of the BNO powders. Crystallite size impacts

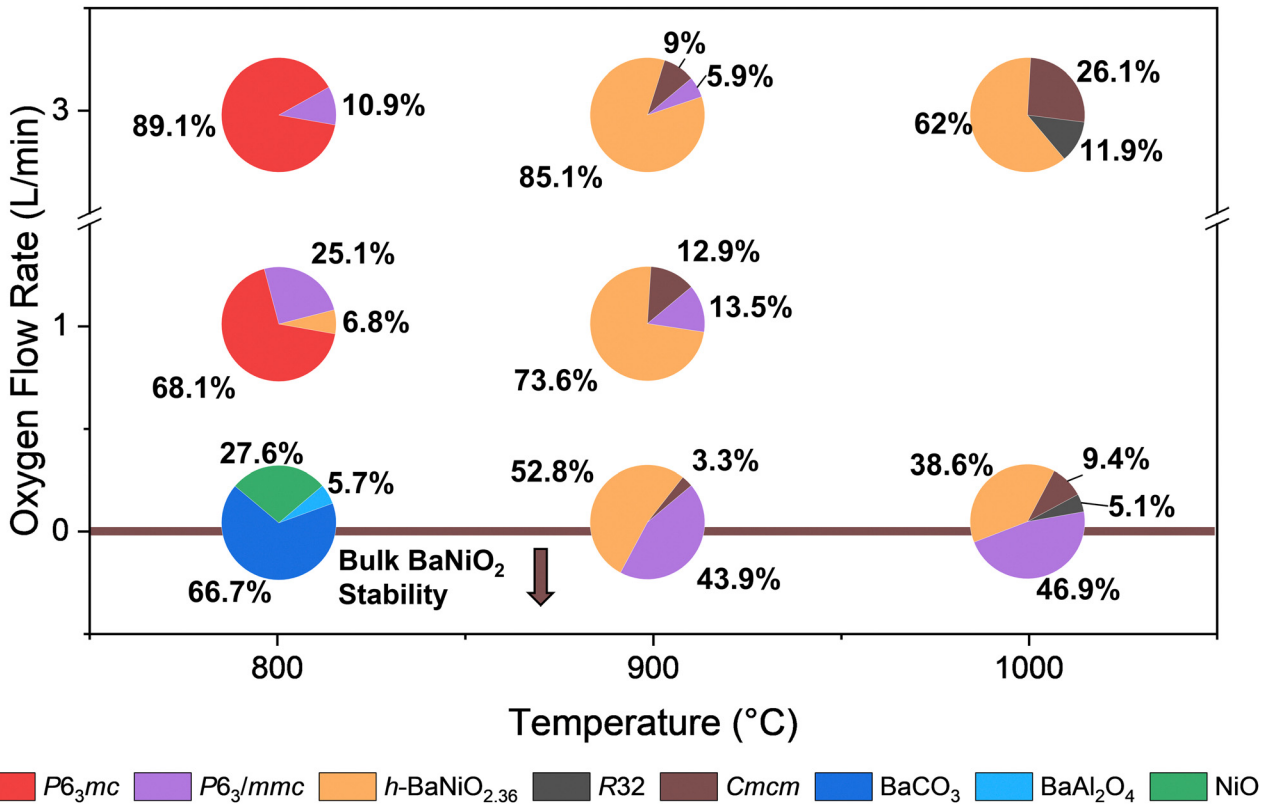

Fig. 3 Rietveld refinement derived phase percentages of BNO phases as a function of temperature and oxygen flow rate. Each pie chart is labeled with the phase percentages of the BNO phases calculated from the diffraction data in Fig. S2–S4. Since calcination at 800 °C under 0 L min^{-1} of flowing O_2 did not result in BNO phase formation, the pie chart is labelled with the relative phase percentages of $BaCO_3$, $BaAl_2O_4$, and NiO. The figure is overlayed with the stability of NiO·BaO ($BaNiO_2$, brown line) [adapted from ref. 33]. The area below the brown line represents the conditions in which $BaNiO_2$ is stable.

oxygen sensitivity, relevant to catalysis and oxygen sensing applications, so understanding how processing parameters such as temperature and oxygen flow rate affect crystallite size is critical.[35–37] The crystallite size of the predominant BNO phase was determined using the Scherrer equation from the (101) diffraction peak for the $P6_3/mmc$ (at 26.03°) and the $P6_3mc$ phases, and the (110) diffraction peak for the h-$BaNiO_{2.36}$ phase (at 31.30°). The average crystallite sizes for the BNO powders are summarized in Table S2. Increasing the oxygen flow at 800 °C (powders predominantly made of the $P6_3mc$ phase) results in an increase in the crystallite size from 23 nm to 34 nm. Increasing calcination temperature also impacts crystallite size, albeit to a far lesser extent than oxygen flow, where raising the temperature from 900 °C to 1000 °C in static air only increased the crystallite size from 26 nm to 27 nm (in the predominant phase $P6_3/mmc$). At higher oxygen flow rates (3 L min^{-1}), however, increasing the calcination temperature from 900 °C to 1000 °C increased the crystallite size from 35 nm to 39 nm (predominant phase h-$BaNiO_{2.36}$). This increase in crystallite size is in agreement with previous literature on similar ABO_3 materials, such as $BaTiO_3$ and $La_{1-x}Sr_xMnO_3$.[38,39] The larger crystallites are attributed to the promotion of diffusion with increasing temperature. The reduction in crystallite size with decreasing oxygen flow rate is likely caused by the formation of oxygen vacancies as the oxygen stoichiometry decreases. For example, it has previously been seen that the particle size of WO_3 powders prepared by a plasma arc gas condensation technique was observed to decrease with increasing Ar/O_2 ratio (decreasing oxygen partial pressure) and decreasing oxygen stoichiometry.[40] Since both calcination temperature and oxygen partial pressure influence crystallite size, it is essential to consider these processing parameters when tailoring the BNO phase and particle size.

Understanding the impact of oxygen flow rate and temperature on the morphology of the BNO powders is important as morphology influences catalytic reactivity, stability, and selectivity of the material.[41,42] As shown in the FESEM micrographs in Fig. 4, calcining the BNO powders at 800 °C results in a porous powder morphology. Increasing the oxygen flow from 1 to 3 L min^{-1}, while maintaining the temperature at 800 °C, increases the interconnectivity of the BNO powders. There is an increase in particle agglomeration for those samples.

Upon increasing the calcination temperature from 800 to 1000 °C, the powder microstructure changes from a spongy to a dendritic morphology. The morphology transition with increasing temperature coincides with the change in phase from $P6_3mc$ to h-$BaNiO_{2.36}$ and the loss of secondary phases within the powder. When comparing the crystallite size determined by the Scherrer equation to the particle sizes observed in the FESEM micrographs in Fig. 4, it is evident that the particle size is much larger than the calculated crystallite size. Differences in the crystallite size from XRD and particle size analysis observed *via* SEM have previously been seen in $La_{1-x}Sr_xMnO_3$ nano-powders where the difference was ascribed to agglomeration of multiple crystallites during particle formation.[39] Furthermore, the calcination temperature used for the BNO powders here are similar to the sintering temperatures used for $BaTiO_3$.[43] Thermogravimetric analysis (TGA) measurements up to 1000 °C (Fig. S6) were conducted on BNO powders which were calcined at 800 °C in 3 L min^{-1} of oxygen. The observed stabilization in mass

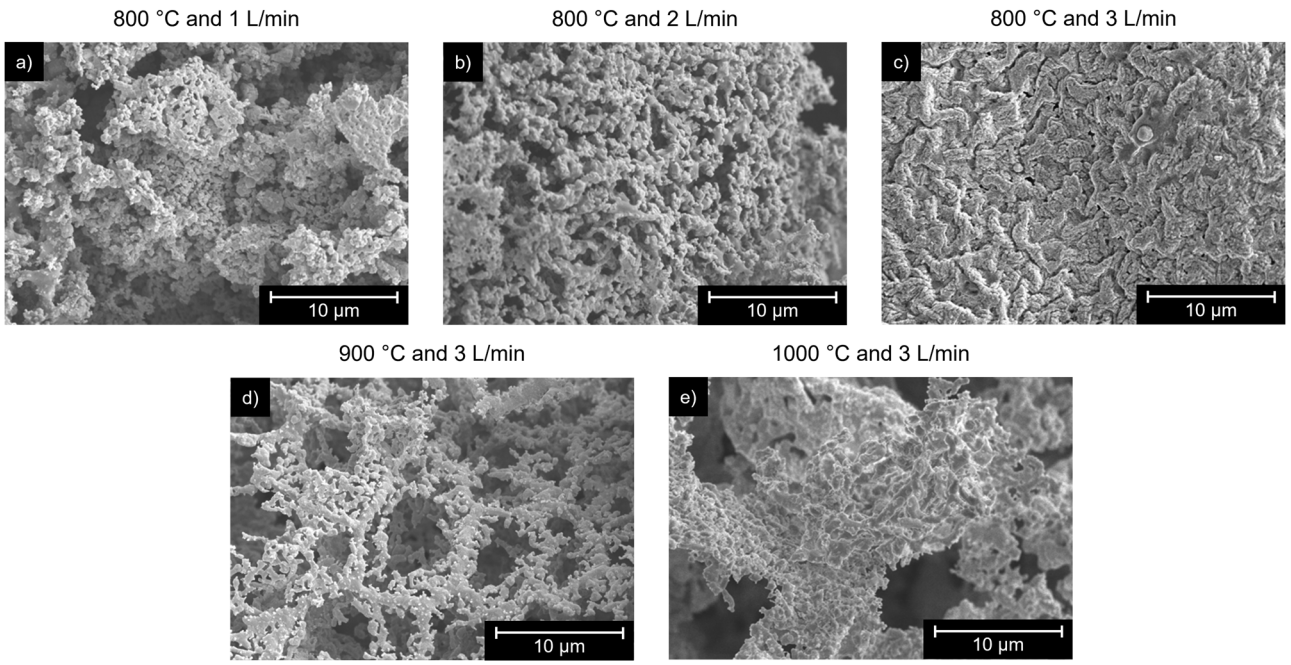

Fig. 4 SEM micrographs of BNO powders illustrating the change in morphology with increasing temperature and oxygen flow rate. (a) Powder calcined at 800 °C under 1 L min^{-1} of oxygen. (b) Powder calcined at 800 °C under 2 L min^{-1} of oxygen. (c) Powder calcined at 800 °C under 3 L min^{-1} of oxygen. (d) Powder calcined at 900 °C under 3 L min^{-1} of oxygen. (e) Powder calcined at 1000 °C under 3 L min^{-1} of oxygen.

change for BNO powders at 1000 °C suggests that the sintering temperature occurs at or near 1000 °C. Therefore, the difference in crystallite size and particle size observed in the BNO powders is due to the onset of agglomeration and sintering. Fundamentally, the ability to control powder morphology through the modulation of calcination temperature and atmosphere is beneficial for catalytic and oxygen sensing applications.

Effects of processing conditions on stoichiometry

While the XRD results provide insight into the phase formation in BNO, it is not yet determined what range of stoichiometries accompany the transition between phases. Here, energy dispersive X-ray spectroscopy (EDS) is performed to elucidate the impact of calcination temperature and oxygen flow rate on the stoichiometry of the BNO powders. The average stoichiometry of each of the BNO powders is shown in Table 1. Increasing calcination temperature, at a constant flow rate of 3 L min^{-1}, decreases the oxygen stoichiometry of the powders from 2.76 to 2.25. Decreasing oxygen flow, with a constant calcination temperature of 800 °C, does not significantly impact the oxygen content of the powders. These results highlight the greater impact of higher temperatures in promoting the formation of oxygen vacancies over the range of conditions covered in this study. Furthermore, decreasing the oxygen flow rate at 900 °C and 1000 °C did not show a change in oxygen stoichiometry (within the ±5% error associated with EDS).

These results agree with previous literature on calcination of similar ABO_3 materials where increasing calcination temperature was found to decrease oxygen stoichiometry (increase formation of oxygen vacancies) due to a decrease in the oxygen activity of the calcination atmosphere.[44] Ultimately, the EDS results in Table 1 illustrate how BNO can be synthesized over a range of stoichiometries and suggests that a range of Ni oxidation states can be accessed just by changing calcination temperature.

Taken collectively, our results demonstrate that temperature plays a more significant role in directing the phase formation pathways of BNO and the resulting stoichiometry. Based on the comparison of the results in Table 1 and Fig. 1 and 2, the predominant role that oxygen flow plays in the stabilization of BNO is in reducing the stability of $BaCO_3$ and NiO. The reduction in the relative phase percentage of $BaCO_3$ suggests that calcination in flowing oxygen will be critical for other ABO_3 type oxides that originate from XCO_3 precursors such as $BaTiO_3$.[45]

For selecting between BNO phases, oxygen flow has a more nuanced role. Given that barium consistently forms in the Ba^{2+} oxidation state, any reduction in O^{2-} necessitates a corresponding decrease in the average Ni oxidation state to maintain charge neutrality. Varying the Ni oxidation state, in turn, alters the electronic structure. In addition, changes in Ni oxidation state can also lead to phase transitions, as the *R*32, *Cmcm*, and it is likely that the h-$BaNiO_{2.36}$ phases have longer Ni–O bonds to better accommodate lower Ni oxidation states. Changes in the crystal structure and stoichiometry will also impact the functional properties, from inducing piezoelectricity upon transitioning into a non-centrosymmetric phase, such as the *R*32 or $P6_3mc$ phases, or transition from insulating to metallic with increased oxygen vacancies. For example, changes in oxygen stoichiometry, due to introduction of oxygen vacancies, were shown to modulate the piezoelectric and ferroelectric response of $Na_xBa_yTiO_3$–$BaTi_{0.5}Ni_{0.5}O_3$.[46] Furthermore, changing the Ni oxidation state of octahedrally complexed Ni ions will change the e_g orbital filling, which has previously been shown to impact the catalytic activity.[14,47] Thus, the ability to tune the range of Ni oxidation states over such a broad range makes BNO particularly interesting for OER catalysis and oxygen sensors.[48] As catalytic activity is also governed by the surface area of active sites, changes in both crystallite size and morphology can result in variations in catalytic activity, as seen in $LaFeO_3$.[49] Porous morphologies could also be beneficial, as was demonstrated in $LaFeO_3$ enhanced gas detection of ethanol while the formation of oxygen vacancies through Ca doping of $LaFeO_3$ improved gas sensitivity and recyclability.[50] Ultimately, this work elucidates the impact of calcination temperature and atmosphere on the phase, stoichiometry, crystallite size, and morphology of BNO powders, illustrating the importance of monitoring these processing parameters when tailoring BNO for applications in catalysis, gas sensing, and piezoelectrics.

Table 1 Stoichiometric ratios of powders as determined by EDS

Temperature (°C)	Flow rate (L min^{-1})	Ba	Ni	O
800	1	1	0.86	2.72
800	2	1	0.93	2.68
800	3	1	0.93	2.76
900	0	1	0.92	2.44
900	3	1	0.86	2.44
1000	0	1	0.91	2.24
1000	3	1	0.96	2.25

Conclusions

In conclusion, this work demonstrates that calcination temperature and oxygen flow rate are powerful levers for tuning the crystal structure, oxygen stoichiometry, crystallite size, and morphology in BNO powders. The results from this study highlight the importance of temperature and atmosphere during the calcination of BNO powders synthesized through the sol–gel solution processing method. Calcination at 800 °C in flowing oxygen stabilized predominantly the $P6_3mc$ phase of BNO, while higher temperatures in static air favored the centrosymmetric $P6_3/mmc$ BNO phase. Remarkably, introducing oxygen flow during calcination above 800 °C resulted in powders that exhibited predominantly the rare h-$BaNiO_{2.36}$ phase. Through elucidating the role of temperature and oxygen flow rate in the phase formation of BNO, this work further develops the processing-structure relationship of BNO enabling access to a wide phase space, including oxygen deficient compositions, for use in catalysis, gas sensing, and piezoelectrics. Furthermore, we show that varying the calcination temperature and atmosphere dictates the powder morphology – from porous sponge like and dendritic morphologies – offering

further control over surface area important for enhancing the catalytic activity oxygen adsorption for sensing applications. Ultimately, this study provides a framework for selectively engineering BNO through the variation of calcination temperature and oxygen flow rate, to control the phase formation pathway in order to tailor BNO for a wide application space.

Author contributions

The manuscript was written through contributions of all authors. All authors have given approval to the final version of the manuscript. I. C. G. synthesized the powders and performed XRD, EDS, and SEM measurements. I. C. G. wrote the manuscript with support from A. M. Ö. and L. M. G. L. M. G. led the project and obtained the funding.

Conflicts of interest

There are no conflicts to declare.

Data availability

Data for this article, including XRD, EDS, and SEM data are available at the Open Science Framework data repository at https://doi.org/10.17605/OSF.IO/DJBUW.

Supplementary information (SI) is available. The supplementary information includes in-situ XRD data, full 2θ-range XRD patterns with phase-indexed diffraction peaks, FESEM images at multiple length scales, Rietveld refinement statistics and phase weight percentages, particle size distribution analyses, and crystallite sizes derived from XRD. See DOI: https://doi.org/10.1039/d5ma01181g.

Acknowledgements

The authors acknowledge funding support from the Office of Naval Research (ONR) through the Young Investigator Award (YIP, Grant No. N00014-22-1-2389). Portions of this research were carried out at the Georgia Tech Institute for Electronics and Nanotechnology, part of the National Nanotechnology Coordinated Infrastructure (NNCI), supported by the National Science Foundation under Grant ECCS-1542174.

References

1 J. J. Lander, *Acta Crystallogr.*, 1951, **4**(2), 148–156, DOI: 10.1107/S0365110X51000441.
2 Y. Takeda, F. Kanamaru and M. Koizumi, *Acta Crystallogr.*, 1976, **32**, 2464–2466, DOI: 10.1107/S056774087600798X.
3 J. A. Campá, E. Gutiérrez-Puebla, M. A. Monge, I. Rasines and C. Ruiz-Valero, *J. Solid State Chem.*, 1994, **108**(2), 230–235, DOI: 10.1006/jssc.1994.1036.
4 H. Krischner, K. Torkar and B. O. Kolbesen, *J. Solid State Chem.*, 1971, **3**(3), 349–357, DOI: 10.1016/0022-4596(71)90070-3.
5 A. Jain, S. P. Ong, G. Hautier, W. Chen, W. D. Richards, S. Dacek, S. Cholia, D. Gunter, D. Skinner, G. Ceder and K. A. Persson, *APL Mater.*, 2013, **1**(1), 011002, DOI: 10.1063/1.4812323.
6 M. K. Horton, P. Huck, R. X. Yang, J. M. Munro, S. Dwaraknath, A. M. Ganose, R. S. Kingsbury, M. Wen, J. X. Shen, T. S. Mathis, A. D. Kaplan, K. Berket, J. Riebesell, J. George, A. S. Rosen, E. W. C. Spotte-Smith, M. J. McDermott, O. A. Cohen, A. Dunn, M. C. Kuner, G.-M. Rignanese, G. Petretto, D. Waroquiers, S. M. Griffin, J. B. Neaton, D. C. Chrzan, M. Asta, G. Hautier, S. Cholia, G. Ceder, S. P. Ong, A. Jain and K. A. Persson, *Nat. Mater.*, 2025, 1–11, DOI: 10.1038/s41563-025-02272-0.
7 A. Jain, G. Hautier, S. P. Ong, C. J. Moore, C. C. Fischer, K. A. Persson and G. Ceder, *Phys. Rev. B*, 2011, **84**(4), 045115, DOI: 10.1103/PhysRevB.84.045115.
8 M. Aykol, S. S. Dwaraknath, W. Sun and K. A. Persson, *Sci. Adv.*, 2018, **4**(4), eaaq0148, DOI: 10.1126/sciadv.aaq0148.
9 A. Wang, R. Kingsbury, M. McDermott, M. Horton, A. Jain, S. P. Ong, S. Dwaraknath and K. A. Persson, *Sci. Rep.*, 2021, **11**(1), 15496, DOI: 10.1038/s41598-021-94550-5.
10 A. M. Arévalo-López, M. Huvé, P. Simon and O. Mentré, *Chem. Commun.*, 2019, **55**(26), 3717–3720, DOI: 10.1039/C8CC09610D.
11 M. Retuerto, F. Calle-Vallejo, L. Pascual, P. Ferrer, Á. García, J. Torrero, D. Gianolio, J. L. G. Fierro, M. A. Peña, J. A. Alonso and S. Rojas, *J. Power Sources*, 2018, **404**, 56–63, DOI: 10.1016/j.jpowsour.2018.09.098.
12 M. Arjomand and D. J. Machin, *J. Chem. Soc., Dalton Trans.*, 1975, **0**(11), 1055–1061, DOI: 10.1039/DT9750001055.
13 D. J. Buttrey, J. D. Sullivan and A. L. Rheingold, *J. Solid State Chem.*, 1990, **88**(1), 291–302, DOI: 10.1016/0022-4596(90)90226-N.
14 J. G. Lee, J. Hwang, H. J. Hwang, O. S. Jeon, J. Jang, O. Kwon, Y. Lee, B. Han and Y.-G. Shul, *J. Am. Chem. Soc.*, 2016, **138**(10), 3541–3547, DOI: 10.1021/jacs.6b00036.
15 M. De Jong, W. Chen, H. Geerlings, M. Asta and K. A. Persson, *Sci. Data*, 2015, **2**(1), 150053, DOI: 10.1038/sdata.2015.53.
16 J. J. Lander and L. A. Wooten, *J. Am. Chem. Soc.*, 1951, **73**(6), 2452–2454, DOI: 10.1021/ja01150a013.
17 J.-Y. Choi, J.-H. Cho, J.-W. Sun, H.-P. Kim, J. Ryu, Y. E. Durmus, H. Tempel, R.-A. Eichel and W. Jo, *Mater. Today Chem.*, 2023, **32**, 101645, DOI: 10.1016/j.mtchem.2023.101645.
18 J. G. Lee, H. J. Hwang, O. Kwon, O. S. Jeon, J. Jang and Y.-G. Shul, *Chem. Commun.*, 2016, **52**(71), 10731–10734, DOI: 10.1039/C6CC05704G.
19 D. Navas, S. Fuentes, A. Castro-Alvarez and E. Chavez-Angel, *Gels*, 2021, **7**(4), 275, DOI: 10.3390/gels7040275.
20 L. Predoana, B. Malic, M. Kosec, M. Carata, M. Caldararu and M. Zaharescu, *J. Eur. Ceram. Soc.*, 2007, **27**(13), 4407–4411, DOI: 10.1016/j.jeurceramsoc.2007.02.161.
21 C.-F. Chen, G. King, R. M. Dickerson, P. A. Papin, S. Gupta, W. R. Kellogg and G. Wu, *Nano Energy*, 2015, **13**, 423–432, DOI: 10.1016/j.nanoen.2015.03.005.

22 V. Torregrosa-Rivero, M.-S. Sánchez-Adsuar and M.-J. Illán-Gómez, *Nanomaterials*, 2022, **12**(2), 219, DOI: 10.3390/nano12020219.
23 D. E. Newbury and N. W. M. Ritchie, *Scanning*, 2013, **35**(3), 141–168, DOI: 10.1002/sca.21041.
24 A. Kern and W. Eysel, ICDD Grant-in-Aid, 1993, in *International Centre for Diffraction Data, Powder Diffraction File*, 1993.
25 K. Martin and G. McCarthy, *Reference X-ray Diffraction Patterns; ICDD Grant-in-Aid Contribution*, North Dakota State University, Fargo, ND, 1991.
26 I. C. Graham, K. Chuong, M. B. Frye, A. M. Österholm and L. M. Garten, *J. Mater. Res.*, 2026, **41**, 208–219, DOI: 10.1557/s43578-025-01668-7.
27 K. Bakken, V. H. Pedersen, A. B. Blichfeld, I.-E. Nylund, S. Tominaka, K. Ohara, T. Grande and M.-A. Einarsrud, *ACS Omega*, 2021, **6**(14), 9567–9576, DOI: 10.1021/acsomega.1c00089.
28 M. Okada, K. Takahashi and T. Mouri, *J. Power Sources*, 1997, **68**(2), 545–548, DOI: 10.1016/S0378-7753(97)02599-8.
29 K.-S. Park, S.-H. Park, Y.-K. Sun, K.-S. Nahm, Y.-S. Lee and M. Yoshio, *J. Appl. Electrochem.*, 2002, **32**(11), 1229–1233, DOI: 10.1023/A:1021606712486.
30 O. El-Sayed, W. M. Mousa, A. Zeinert, A. Lahmar, M. El Marssi and I. K. Battisha, *Adv. Nat. Sci.: Nanosci. Nanotechnol.*, 2020, **11**(1), 015015, DOI: 10.1088/2043-6254/ab798d.
31 Q. Ji, L. Bi, J. Zhang, H. Cao and X. S. Zhao, *Energy Environ. Sci.*, 2020, **13**(5), 1408–1428, DOI: 10.1039/D0EE00092B.
32 K. Jangam, K. Patil, S. Balgude, S. Patange and P. More, *J. Phys. Chem. Solids*, 2021, **148**, 109700, DOI: 10.1016/j.jpcs.2020.109700.
33 K. A. Denault, J. Brgoch, S. D. Kloß, M. W. Gaultois, J. Siewenie and K. Page, *ACS Appl. Mater. Interfaces*, 2015, **7**(13), 7264–7272, DOI: 10.1021/acsami.5b00445.
34 J. J. Lander, *J. Am. Chem. Soc.*, 1951, **73**(6), 2450–2452, DOI: 10.1021/ja01150a012.
35 T. M. Nyathi, N. Fischer, A. P. E. York and M. Claeys, *Faraday Discuss.*, 2017, **197**(0), 269–285, DOI: 10.1039/C6FD00217J.
36 M. Baumung, F. Schönewald, T. Erichsen, A. Volkert and C. Risch, *Sustainable Energy Fuels*, 2019, **3**(9), 2218–2226, DOI: 10.1039/C8SE00551F.
37 Y. Uetake, S. Mouri, S. Haesuwannakij, K. Okumura and H. Sakurai, *Nanoscale Adv.*, 2021, **3**(5), 1496–1501, DOI: 10.1039/d0na00951b.
38 P.-J. Chang, M.-S. Chen, C.-H. Cheng, Y.-J. Chiou, C.-Y. Chen, C.-Y. Su and C.-K. Lin, *Materials*, 2024, **17**(11), 2701, DOI: 10.3390/ma17112701.
39 D. Hung Manh, T. T. N. Nha, L. T. H. Phong, P. Hong Nam, T. Dang Thanh and P. Thanh Phong, *RSC Adv.*, 2023, **13**(36), 25007–25017, DOI: 10.1039/D3RA04018F.
40 C.-Y. Su, C.-K. Lin, T.-K. Yang, H.-C. Lin and C.-T. Pan, *Int. J. Refract. Met. Hard Mater.*, 2008, **26**(5), 423–428, DOI: 10.1016/j.ijrmhm.2007.09.006.
41 T. Long, D. Song, Y. Zhou, X. Yu, X. Wang, C. Li, H. Chen, G. Li and F. He, *ACS Appl. Mater. Interfaces*, 2025, **17**(14), 20590–20612, DOI: 10.1021/acsami.5c03046.
42 M. Humayun, Z. Li, M. Israr, A. Khan, W. Luo, C. Wang and Z. Shao, *Chem. Rev.*, 2025, **125**(6), 3165–3241, DOI: 10.1021/acs.chemrev.4c00553.
43 N. Sharma, A. Gaur and U. Kr Gaur, *Ceram. Int.*, 2014, **40**(10, Part B), 16441–16448, DOI: 10.1016/j.ceramint.2014.07.153.
44 Y. Zhu, X. Liu, S. Jin, H. Chen, W. Lee, M. Liu and Y. Chen, *J. Mater. Chem. A*, 2019, **7**(11), 5875–5897, DOI: 10.1039/C8TA12477A.
45 M. T. Buscaglia, V. Buscaglia and R. Alessio, *Chem. Mater.*, 2007, **19**(4), 711–718, DOI: 10.1021/cm061823b.
46 H. Xiao, Y. Wang, N. Jiao, Y. Guo, W. Dong, H. Zhou, Q. Li and C. Sun, *Adv. Electron. Mater.*, 2019, **5**(10), 1900407, DOI: 10.1002/aelm.201900407.
47 J. Suntivich, K. J. May, H. A. Gasteiger, J. B. Goodenough and Y. Shao-Horn, *Science*, 2011, **334**(6061), 1383–1385, DOI: 10.1126/science.1212858.
48 J. T. Mefford, X. Rong, A. M. Abakumov, W. G. Hardin, S. Dai, A. M. Kolpak, K. P. Johnston and K. J. Stevenson, *Nat. Commun.*, 2016, **7**(1), 11053, DOI: 10.1038/ncomms11053.
49 S. Thirumalairajan, K. Girija, Y. Hebalkar, N. Mangalaraj, D. Viswanathan and C. Ponpandian, *RSC Adv.*, 2013, **3**(20), 7549–7561, DOI: 10.1039/C3RA00006K.
50 P. M. Bulemo and I.-D. Kim, *J. Korean Ceram. Soc.*, 2020, **57**(1), 24–39, DOI: 10.1007/s43207-019-00003-1..